AIAA JOURNAL
Vol. 49, No. 5, May 2011

Flow Control by Dynamic Vane Vortex Generators Based on Piezoceramic Actuators

Thomas Barth* and Peter Scholz†
Braunschweig Institute of Technology, 38106 Braunschweig, Germany
and
Peter Wierach‡
DLR, German Aerospace Center, 38106 Braunschweig, Germany

DOI: 10.2514/1.J050378

This paper describes a study of dynamical vane vortex generators in a flow over a flat plate. Fluidic vortex generators are more effective when operated dynamically. Thus, it is the aim of this study to find out whether mechanical vortex generators are also superior under dynamic operating conditions. The motion of the vortex generators is generated by piezoceramic actuators constructed in a bimorph configuration, which consists of a carbon-fiber bar covered with piezoceramic face actuators. The actuators exploit the longitudinal piezoelectric effect (d_{33} effect), they are operated in resonance to reach the required displacement and generate a sinusoidal motion of the vortex generators. Vortex generators and actuators were integrated into a flat plate in a low-speed wind tunnel. A stereo particle image velocimetry system was used to record phase-locked flowfields that were analyzed using vortex classification methods. It was found that the transient development of the vortex core position and circulation is very different from that of static vanes. While vortices from static vortex generators are able to survive over a considerable distance, the vortices from dynamically driven ones decay faster. It is argued that the dynamic vortices have a greater ability to reorganize the momentum in the turbulent boundary layer.

Nomenclature

b	=	widths (e.g., width of actuator bar), mm
d_{33}, d_{31}	=	piezoelectric constants, pm/V
E_C	=	tensile modulus of the ceramics, GPa
E_S	=	tensile modulus of substrate material, GPa
E_3	=	electrical field strength, 3-direction is the direction of the field, V/m
f	=	frequency of oscillation, Hz
f_1	=	first eigenfrequency, Hz
G_{12}	=	shear modulus, GPa
h	=	height of vane or generally thicknesses or sizes in z direction, mm
h_C	=	thickness of piezoceramics, mm
h_S	=	thickness of the passive substrate, mm
L	=	spacing between two vanes, mm
l	=	lengths (e.g., length of one vane), mm
m	=	mass, kg
m_E	=	additional mass at the tip of the bar, kg
Re_x	=	Reynolds number based on freestream velocity and upstream length
Re_θ	=	Reynolds number based on edge velocity and momentum thickness
Sr	=	Strouhal number, see Eq. (1)
$U_{\max}$	=	maximum positive operation voltage, V
$U_{\min}$	=	minimum negative operation voltage, V
U_{pp}	=	dynamic peak-to-peak supply voltage, V
U_{stat}	=	static supply voltage, V
u, v, w	=	velocity components in x, y, and z directions, m/s
$\hat{u}$, $\hat{v}$, $\hat{w}$	=	periodic fluctuation components (only $\hat{u}$ used herein), m/s
u_τ	=	shear stress velocity, m/s
u_∞	=	freestream flow velocity, m/s
u', v', w'	=	stochastic fluctuation components (only u' used herein), m/s
w_{dyn}	=	displacement of the actuator bar in dynamic operation, mm
w_0	=	deflection of bar with static supply voltage, mm
x, y, z	=	spatial directions, x is streamwise, z is wall normal, mm
x^+, y^+, z^+	=	spatial dimensions in wall units (only z^+ used herein)
z_{stat}	=	position of the vortex core from statically deployed vortex generators, mm
β	=	ratio of tensile moduli; Eq. (2)
β_{pd}	=	skew angle of vortex generator relative to base flow direction, deg
Γ_{stat}	=	circulation of the vortex from statically deployed vortex generators
Γ_x	=	circulation around x axis; see Eq. (7)
$\Delta(X)$	=	experimental uncertainty of the value X, $[X]$
δ	=	boundary-layer thickness, mm
η	=	ratio of thicknesses, Eq. (2)
θ	=	momentum deficit thickness of the boundary layer, mm
Λ	=	average peak-to-peak free strain, μm/V
λ	=	width of a common flow-up configuration, mm
λ_1	=	eigenvalues of the expression in Eq. (5)
ν_{12}, ν_{21}	=	Poisson's ratios
φ	=	phase angle of the periodical process, deg
ω_x	=	vorticity around x axis, 1/s

Received 3 December 2009; revision received 3 March 2010; accepted for publication 12 December 2010.

*Research Assistant; currently Helmholtz-Zentrum Dresden-Rossendorf; t.barth@fzd.de.

†Research Engineer, Institute of Fluid Mechanics; P.Scholz@tu-bs.de. Member AIAA.

‡Research Engineer, Institute of Composite Structures and Adaptive Systems; Peter.Wierach@dlr.de.

I. Introduction

VORTEX generators are typically small triangular shaped vanes that are placed on an aerodynamic body. Because of its geometry this type of vane vortex generator (VVG) creates vortices that are aligned in the flow direction. These streamwise vortices transport momentum from the free stream into the boundary layer. Thus, the

near-wall flow is accelerated, energized and turbulent separation can be delayed. The effect was first discovered in 1948 by McCurdy [1], and since then the application of vortex generators to prevent flow separation has been investigated continuously by both experimental and numerical tools [2–6]. It is well known that they can effectively delay stall and thereby increase the maximum lift of airfoils; e.g., micro vortex generators on the flap of a multi-element high-lift system can increase the maximum lift coefficient [7]. However, VVGs typically suffer from the fact that they produce additional drag in cruise flight and are therefore usually a makeshift, not a regular, high-lift device.

This disadvantage might be circumvented by producing the vortex with a fluidic device: e.g., with a jet emanating from a skewed and/or pitched hole or slot. This kind of device is often called vortex generator jet (VGJ), it was first used with the intention to control a shock-induced separation [8,9] and then adopted for the control of a pressure-induced separation [10,11]. McManus et al. [12] found that VGJs should be operated dynamically, because the mass flow can be reduced, but the effectiveness is even superior. The exact mechanism is still not exactly known, nevertheless it is generally accepted that the dynamically driven VGJs are more effective than static ones, [13,14]. A hypothesis stated that the increased efficiency is due to the fact that the pulsing stimulates additional eddies [12]. Other presumptions are that the vortices descent deeper into the boundary layer during the inactive part of the period, which therefore leads to the increases in the efficiency [15], or are based on the observation that the vortex is intensified during the transient phases of the pulsing [16]. Furthermore, it was shown [17] that the increased mixing of such dynamic vortex generators does not primarily act on turbulence scales, but that it is a large-scale momentum transport phenomenon. It was also stated that the driving frequency f and duty cycle Δ are less significant than the injection time as the most relevant parameter for pulsed vortex generator jets [5]. This is consistent with the suggestion that the transient phases of the pulsing are more effective and thus the VGJ should be operated with a certain combination of frequency and duty cycle. However, when sinusoidal motions are applied to dynamic VVGs, the injection time is directly coupled to only the frequency, because of the fixed duty cycle.

Cattafesta et al. [18] used a unimorph flap design with a piezoelectric actuator to excite the shear layer of a backward facing step. They found a considerable amplification of the wall-normal velocity component of their flap even in the case of quasi-static excitation, meaning that the frequency of the flap-movement is smaller than the relevant timescales of the flow.

Dynamically driven vane-type vortex generators have been recently investigated by two teams [19,20]. In both studies it was found that the behavior is very different from static VVGs. However, both come to different conclusions and the effect of the dynamic VVGs was assessed mainly in terms of integral values such as pressure recovery or overall lift, respectively.

In summary, fluidic devices seem more interesting from a practical point of view, but vortex generator jets are typically limited by the maximum frequency, because the available valves start to exhibit a nonflat frequency response. During real applications, this might be circumvented with specially tuned systems. However, for basic research on such devices, it would be interesting to construct a system with a large range of possible frequencies.

For this feasibility study an experimental investigation has been undertaken to explore if some of the observations described above for vortex generator jets are reproducible with dynamically driven mechanical vane-type vortex generators. The bending actuators that drive the dynamic VVGs consisted of a passive-substrate material covered on both sides with thin MFC actuators operating in the longitudinal d_{33} direction. Above the first bending resonance frequency the deflection of the actuator decreases rapidly because higher mode shapes are excited. Therefore, the eigenfrequency of the actuator has to be set to the upper limit of the required frequency range. Stiff materials with a high Young's modulus result in a high eigenfrequency; hence, the substrate of the actuator was made of a high-modulus carbon-fiber composite (CFC). Because of the high stiffness of the substrate, the static deflection of the actuator was small, sufficient deflections were only achieved when the actuator was driven at its eigenfrequency. To tune the eigenfrequency to the desired operating point, clamps with different weights were mounted on the bar.

II. Design of the Actuation System

A. Preliminary Design Basis

The parameters that defined the design specifications for the actuators were the effective displacement of the actuators and the operating frequency. It was specified that the effective displacement of the actuators should be around $w_{\mathrm{dyn}} = 2$ mm and the operating frequency should be $f \in 100$–500 Hz. This section will state the reasons for these choices.

As the best basic design, a one-sided clamped cantilever beam was chosen that is bent up and down by means of piezoceramic actuators that are applied at the top and bottom sides (see Sec. III.A). One part of the discussion was the question of whether or not to use a mechanical way to enlarge the motions of the bending bar (e.g., something similar to the compliant displacement-amplification mechanism used by Osborn et al. [19]). Because of the prediction that mechanically moving parts will seriously decrease the eigenfrequency, it was decided not to consider such systems. Therefore, the required displacement of the bending cantilever beam (w_{dyn}) must equal the height of the vortex generator vanes h, which in the next step must be defined on the basis of a literature research.

Godard and Stanislas [4] provided the basis for the choice of h, where an overview of some different vane VGs is presented. The different heights that were tested range from $h/\delta \approx 0.12$ to $h/\delta \approx 0.47$. For the experiments described herein, a boundary-layer thickness of $\delta \approx 10$ mm was expected [15,21]. Although Godard and Stanislas [4] favor heights of $h/\delta = 0.37$ for counter-rotating triangular vanes, it was decided to use slightly smaller VGs herein, since it was foreseeable that large deflections will lead to more and more intricate structural design process, which in turn would limit the frequency range. Therefore, a value of $h/\delta = 0.2$ or $h = 2$ mm was chosen as the design goal, which is on the lower end of typical heights presented in the above cited reference, but it is still within the comparable range. Consequently the bending cantilever beam must deliver an effective displacement of $h = w_{\mathrm{dyn}} = 2$ mm.

The second requirement was set with regard to the results of Ortmanns et al. [16]. They performed experiments in a water tunnel with a turbulent boundary layer with similar properties as the one that will be described herein. They conclude that the timescale of the transient phase during the startup of the vortex is $t \in 0.1$–0.24 s. Hence, favorable frequencies would range over $f \in 2$–5 Hz (in water). This can be transformed to air using the dimensionless Strouhal number:

$$Sr = \frac{f \cdot \delta}{u_\infty} \tag{1}$$

Based on these suppositions, favorable Strouhal numbers in the turbulent boundary layer are $Sr \approx 0.1$–0.2, which is consistent to the $Sr = 0.16$ used by Cattafesta et al. [18].

A link might be established to studies to the bursting frequencies in the inner part of turbulent boundary layers, which are in that range. For example, Wei and Ning [22], who summarized contributions of Kim et al. [23], Blackwelder and Haritonidis [24], and others who also contributed their own measurements, although some of these references arrive at different conclusions with regard to the dependency of the frequency scale with Reynolds number and viscosity. They all indicate that the bursting frequency of the turbulent boundary layer is $Sr \approx 0.2$ for turbulent boundary layers with $Re_\theta = 1000$ when Sr is evaluated according to the macroscopic boundary-layer parameters defined in Eq. (1).

For free shear layers Wu et al. [25] conclude, with a reference to Ho and Huerre [26], that unstable frequencies can be found around $Sr = 0.044$–0.048, where they chose the momentum deficit thickness θ as the characteristic length in Eq. (1) and the mean or center velocity of the shear layer instead of u_∞. If a boundary layer is

thought of as a shear layer with a mean or center velocity of approximately half the freestream velocity u_∞ and with a momentum deficit thickness as expected for the experiments herein, this would result in frequencies of around $f \in 260$–280 Hz.

In the turbulent boundary layer (in air) that is expected here, this would mean that it is particularly interesting to cover frequencies in the range $f \in 100$–300 Hz. To cover this range securely the design goal was set to $f \in 100$–500 Hz. It should be noted that reaching this frequency range was one of the main motivations for the work described here, because even the fastest commercially available valves (to the authors knowledge) that can be used to design systems for fluidic vortex generator jets are limited to maximum frequencies around $f_{\max} \approx 200$ Hz.

B. Vane Vortex Generators

The aerodynamic design of the VVGs was adapted from Godard and Stanislas [4], who proposed a counter-rotating configuration that was more effective (Fig. 1). The height of the VVGs must equal the maximum actuator deflection and was hence set to $h = 2$ mm. All other parameters were chosen following the publication mentioned above, where all angle values were adopted directly, while all lengths were taken relative to the VG height: skew angle relative to base flow $\beta_{pd} = 18°$, width of a common flow-up configuration $\lambda/h = 6$ or $\lambda = 12$ mm, respectively, length of one VG $l/h = 2$ or $l = 4$ mm, spacing between two vanes $L/h = 2.5$ or $L = 5$ mm.

C. Bending-Bar Actuator

It was decided to realize the requirements with a system composed of a passive-substrate material, covered on both sides with thin-piezoceramic-sheet actuators. The term *passive substrate* is used here, because the substrate does not contribute actively to the bending process. It only provides the required stiffness and strength, while the active piezoceramic introduces the strain that bends the substrate into the required shape.

For piezoceramic actuators, the correlation between electrical field and strain in direction of the electrical field is described by the charge or strain constants d_{31} and d_{33}. The first index specifies the direction of the electrical field and the second index the direction of the used deformation (with respect to a Cartesian coordinate system in which the 3-direction is always the direction of the electrical field). Consequently, the d_{31} constant describes the deformation of the piezoelectric material perpendicular to the electrical field, and d_{33} describes the deformation in the direction of the electrical field (parallel with it). As the d_{33} constant is three times larger than the d_{31} constant a much higher performance can be achieved with a d_{33} mode actuator (though the stiffness in the 3-direction is slightly smaller).

A suitable actuator for this purpose is the so-called macrofiber composite (MFC) actuator [27]. This device is a piezocomposite consisting of piezoceramic fibers with rectangular cross sections, which are embedded in a polymer and provided with surface mounted interdigitated electrodes to generate the in-plane electric field. The combination of the brittle piezoceramic material in a fiber

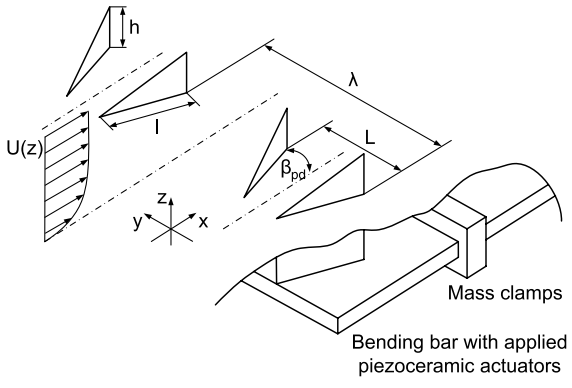

Fig. 1 Basic geometry of the VVGs, nomenclature according to [4], and illustration of the submerged bending bar and the mass clamps.

Table 1 Properties of the MFC actuators used to build up the bending actuator with piezoceramic-sheet thickness $h_C = 0.3$ mm[a]

Property	Value	Unit
Mechanical properties		
Tensile modulus E_C	30.34	GPa
Shear modulus G_{12}	5.52	GPa
Poisson's ratio ν_{12}	0.31	——
Poisson's ratio ν_{21}	0.16	——
Active properties		
Maximum positive operation voltage $U_{\max}$	1500	V
Minimum negative operation voltage $U_{\min}$	−500	V
Piezoelectric constant d_{33}	460	pm/V
Piezoelectric constant d_{31}	460	pm/V
Average peak-to-peak free strain Λ	1600	μm/V

[a]From Smart Material GmbH product brochures (see http://www.smart-material.com/).

like architecture with ductile polymer materials forms a robust and easy to use sheet actuator. A principle drawback of this type of actuator is the very high operating voltage, which in this case ranges from −500 to +1500 V. The maximum negative operation voltage is defined by the coercive field strength of the piezoelectric material. MFC actuators are commercially available from the company Smart Material GmbH, which offers MFCs in different configurations and sizes.[§] For this study MFC actuators with an active length of 85 mm and a width of 57 mm (type M8557-P1) and 28 mm (type M8528-P1) have been used in the construction of the bending actuators. The basic passive and active properties are listed in Table 1.

As the first step in their design, the influence of the geometrical and structural details on different parameters of the bar, namely static displacement and eigenfrequency, have to be determined. To estimate static displacement Monturet and Nogarede [28] presented a simple analytical model, partly referring to the work of Crawley and Anderson, [29]. Introducing the two variables:

$$\beta = \frac{E_C}{E_S} \quad \text{and} \quad \eta = \frac{h_C}{h_S} \tag{2}$$

Neglecting external forces, the static displacement w_0 may then be expressed by:

$$w_0 = 3l^2 \cdot \frac{\beta\eta(1+\eta)}{h_S(1+4\beta\eta+6\beta\eta^2+4\beta\eta^3+\beta^2\eta^4)} \cdot d_{33}E_3 \tag{3}$$

where E_3 is the strength of the electric field and d_{33} is the piezoelectric constant in the relevant direction. E_C and h_C are the tensile modulus and thickness of the piezomaterial and E_S and h_S of the passive substrate, respectively (see Table 1 for the piezos and Table 2 for the different substrates). Furthermore, neglecting the influence of the MFC, the first eigenfrequency f_1 of the bar is computed by [30]:

$$f_1 = \left(\frac{1875}{l}\right)^2 \cdot \frac{h}{2\pi}\sqrt{\frac{E_S}{12\rho_S}} \tag{4}$$

To validate this approach, two test bars were built, mounted onto a fixed support clamp, and measured by a noncontact laser-displacement sensor (Micro-Epsilon optoNCDT 1606). The measurement uncertainty of this instrument is given as $\Delta(w) = \pm 3$ μm. Figure 2 shows the geometrical definitions of the sheet thicknesses and the definition of the displacement w. In the following the displacement with a static voltage will be denoted with the subscript 0 (w_0) and during dynamic operation with dyn (w_{dyn}). To generate the largest possible bending deformation, the top and bottom of the bar are covered with piezoceramic actuators and both are driven with a phase shift of 180°.

[§]Available online at http://www.smart-material.com/.

Table 2 Geometrical and structural data of the different actuators

Data	Aluminum	Carbon-fiber composite	
Geometrical and mechanical data of the passive substrates			
Size ($l \times b \times h_s$), mm	$104 \times 38 \times 1.5$	$120 \times 31 \times 3.5$	$110 \times 67 \times 4$
Density ρ_S, kg/m^3	2700	1580	1580
Relevant tensile modulus E_S, GPa	70	150	150
Thickness h_S, mm	1.5	3.5	4
Computed values for f_1 and w_0			
Eigenfrequency f_1, Hz	114.1	383	502
Static deflection w_0,[a] mm)	1.63	0.17	0.14
Measured values for f_1 and w_0			
Eigenfrequency f_1, Hz	110 ± 1	369 ± 1	403 ± 1
Static deflection w_0,[a] mm	$1.65 \pm 3e-3$	$0.17 \pm 3e-3$	$0.14 \pm 3e-3$

[a]With $U_{stat} = 2$ kV.

Three actuators have been tested, one made with aluminum as the passive substrate ($104 \times 38 \times 1$) and two using CFCs ($120 \times 31 \times 3.5$ and $110 \times 67 \times 4$). The carbon-fiber substrate was manufactured with 16 layers of prepreg material (HexPly 913C-T300J-10-35% prepreg material) with an area weight of 134 g/m^2 in a quasi-isotropic stacking sequence, aligned longitudinally to the bar to maximize the bending stiffness. The prepreg was cured in an autoclave process with 3 bar pressure in a sequence at 90°C for 40 min and 125°C for 60 min. Subsequently, the MFC actuators were bonded onto the substrate materials using a cold-setting epoxy (Loctite Hysol 9466 A&B) that was cured for 12 h at room temperature. The aluminum actuator ($104 \times 38 \times 1$) and the larger CFC actuator ($120 \times 31 \times 3.5$) are the two test cases that will be discussed in the following sections. The details are given in Table 2.

To tune the design methodology, the two test cases were chosen to be very different: a flexible aluminum bar and a very stiff CFC bar. Table 2 shows the computed values for static displacement and eigenfrequency, where w_0 denotes the displacement of the tip of the bar when the piezoceramic sheets are stimulated with a constant voltage of $U_{stat} = 2$ kV. It should be noted here that the maximum positive voltage applicable to these piezoceramics is limited to 1.5 kV (mentioned above). To apply $U_{stat} = 2$ kV and hence generate the largest possible w_0 the actuators were driven here with a very low frequency (1 Hz) between -500 V and $+1.5$ kV, and w_0 is the displacement difference between the two extremum states. An amplifier of the type Trek PZD2000 was used, which had maximum voltages of ± 2 kV and a maximum current of 400 mA.

As expected, the aluminum bar has a high static displacement with a low eigenfrequency, whereas the stiff CFC bar has a low static displacement with a relatively high eigenfrequency. It should be noted that both the eigenfrequency f_1 and the static displacement w_0 are captured by the analytical methods quite accurately.

Figures 3 and 4 show the displacement w_{dyn} versus the frequency f for the two actuators with a constant peak-to-peak excitation of the piezoceramic sheet of $U_{pp} = 500$ V. The plots were generated using a sinusoidal test signal that sweeps the frequencies in the range of $f = 1600$ Hz. Note here that the dynamic peak-to-peak excitation voltage was reduced in this test setup to reduce the reaction forces on the support clamping (will be described later). In the proximity of the eigenfrequency, the dynamic displacement is large. Well below the first eigenfrequency the displacement is similar to the steady case, the movement is quasi-steady. Above the first eigenfrequency the displacement decreases rapidly to very low values, because the force of the piezoceramic actuators is not large enough to accelerate the mass of the beam sufficiently quick. Two conclusions for the design of a suitable actuator can be drawn: First, the eigenfrequency has to be set to the upper limit of the desired frequency range. Second, the static or dynamic displacement far away from the eigenfrequency is not at all high enough to reach the desired displacement of $w_{dyn} = 2$ mm. Only by tuning the eigenfrequency into the desired operating frequency can the actuator reach the intended displacement.

Based on this experience, the final actuator used CFC as the passive-substrate material. The thickness of the bar was redesigned to result in an eigenfrequency of $f_1 \approx 500$ Hz. The change of the displacement w_{dyn} against frequency f for this CFC bar ($110 \times 67 \times 4$) is plotted in Fig. 5. For this an even stiffer bar was used, as the original support clamping support started to disintegrate, named weak support clamping in the figure. Therefore, the experiments were rerun with a stronger support clamp made from stainless steel, which as a result increased the bulk of the wind-tunnel model. Although this bar does not reach the desired eigenfrequency of 500 Hz in the experiments, the obtained frequency was considered

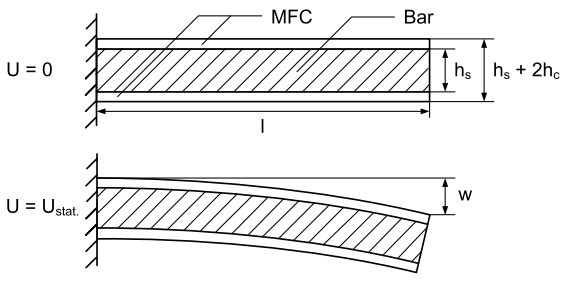

Fig. 2 Geometry of the MFC bar and definition of the displacement w.

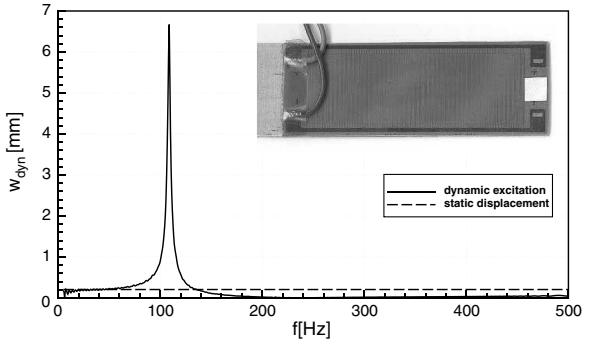

Fig. 3 Displacement w_{dyn} vs frequency f for 104 × 38 × 1 aluminum actuator.

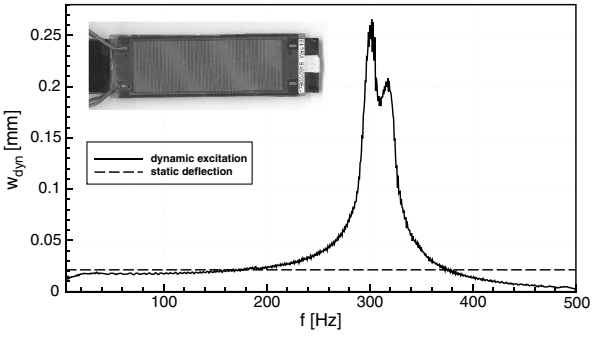

Fig. 4 Displacement w_{dyn} vs frequency f for 120 × 31 × 3.5 CFC actuator .

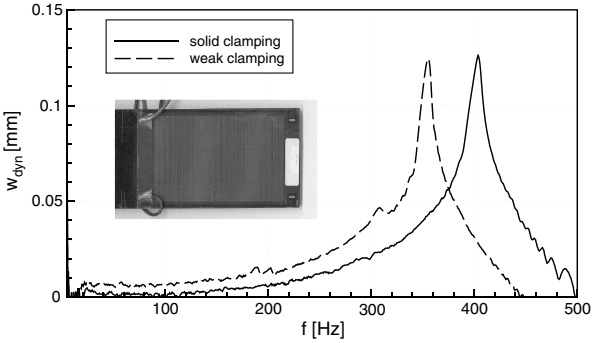

Fig. 5 Displacement w_{dyn} vs frequency f for 110 × 67 × 4 CFC actuator.

acceptable, because further strengthening of the bars would unacceptably increase the size of the actuators and the support clamping.

D. Dynamic Displacement Enlargement

Since the desired displacement can only be generated in resonance, the eigenfrequency of the bar must be tuned to the desired operating point. This was done by applying mass clamps of different weight. For a bending bar with Young's modulus E, mass m_0, and an additional mass m_E, an analytical description for such a problem has been developed [30]. The starting point is a mechanical model consisting of two linear partial differential equations, one for the bending moment at the clamp and one for the inertia force of the added mass m_E at the tip, where the subscript 0 denotes the values without and E the values with an added mass. Solving the determinant of this equation system leads to the following expression:

$$1 + \cosh\lambda_1 l \cdot \cos\lambda_1 l + \frac{m_E}{m_0}\lambda_1 l \cdot (\sinh\lambda_1 l \cdot \cos\lambda_1 l - \cosh\lambda_1 l \cdot \sin\lambda_1 l) = 0 \tag{5}$$

The eigenvalues λ_1 of this equation were computed by a MATLAB solver. Finally, the reduction of the eigenfrequency f_1 is the square ratio of the new and the old eigenvalues:

$$\frac{f_{1,E}}{f_{1,0}} = \left(\frac{\lambda_{1,E}}{\lambda_{1,0}}\right)^2 \tag{6}$$

The reduction of the eigenfrequency is a function of the additional mass relative to the old mass. The characteristic is plotted in Fig. 6. For example, reducing the eigenfrequency of the bar by about 50% requires an additional mass m_E at the tip of $0.6 \cdot m_0$. The additional mass was realized with claws of different mass made from stainless steel that can be fixed to the bar (see Sec. III). An additional degree of freedom exists due to the possibility to vary the position of the mass clamp between tip and the support clamp. By using different combinations of mass, mass clamp position and stimulation voltage, the desired displacement of 2 mm can be generated for any desired frequency up to the first eigenfrequency of the bar itself.

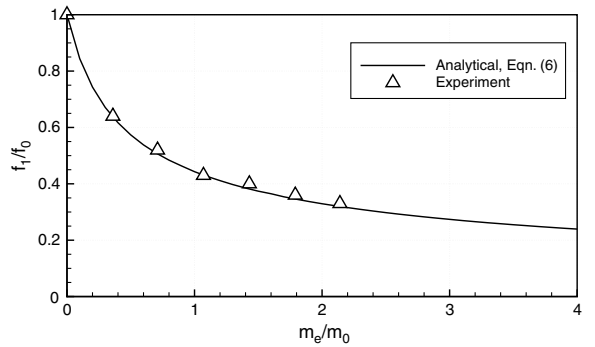

Fig. 6 Reduction of eigenfrequency vs mass ratio m_E/m_0 for bars with additional mass m_E at the tip.

III. Experimental Setup

A. Wind-Tunnel Setup

A flat plate was installed horizontally in a 1.3 m low-speed wind tunnel (Fig. 7) with an open test section. The model has a length of 1 m and is equipped with an elliptical leading edge that has an aspect ratio of 6:1 to suppress destabilizing separations at the leading edge. To absorb structural oscillations stimulated by the operation of the actuators, a system of steel cable stiffeners was connected to the flat plate. The boundary layer was tripped at the leading edge using a strip of sandpaper (grain size 60). The VVGs were located 350 mm downstream of the flat plate's leading edge. The measurements that will be described below were done in the center section of the flat plate, a total number of 26 individual vanes were installed in a spanwise row such that periodicity can be assumed for the center vanes. The vanes are installed on two individual bending bars, each of them driving 13 vanes, respectively. The actuator system was mounted underneath the flat plate (Fig. 8). The VVGs were fixed to the free tip of the active bar and they penetrate through small slits in the plate into the turbulent boundary layer.

The bending-bar supply voltage was tuned for each case such that the tips of the VVGs oscillate between the surface plane and 2 mm above it. For this tuning, the cameras of the particle image velocimetry (PIV) system were used to assess the correct overall deflection and to find the correct time for the reference phase angle $\varphi = 0°$, which is defined herein as the point in time when the VVGs are fully extracted. For the static deflection, the CFC bar was simply bent to the correct position of $h = 2$ mm by using a massive clutch. x is defined here as the streamwise component direction of the undisturbed bulk flow, z denotes the wall-normal component and consequently y is the spanwise direction.

A stereo 3C2D-PIV system [31] was mounted on a separate traverse close to the test section. The double-pulse laser (Quantel

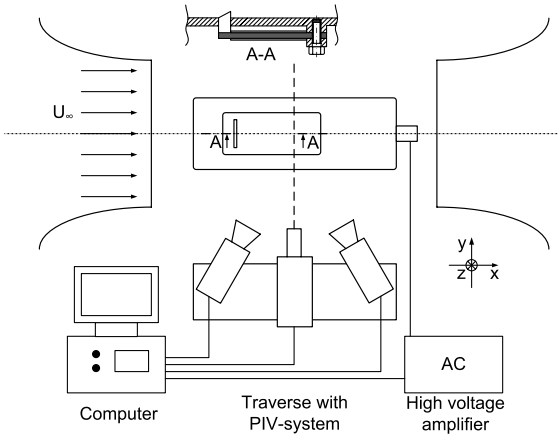

Fig. 7 Experimental setup in the wind tunnel.

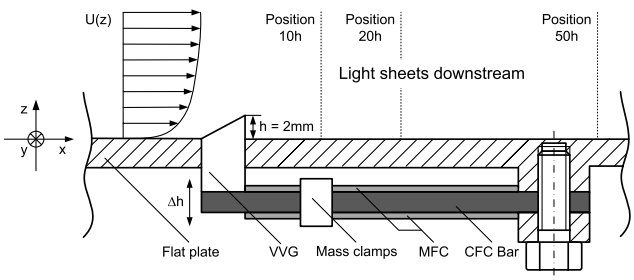

Fig. 8 Sectional view (close-up of cut A-A) of the flat plate, showing the bending bar, the mass clamps, the solid clamping, and the vortex generators penetrating through slits into the boundary-layer flow.

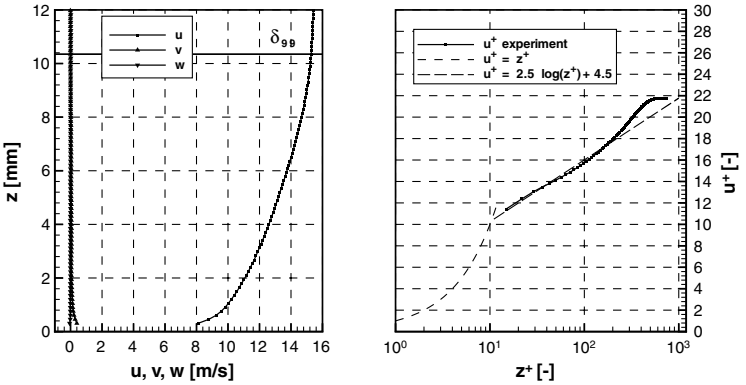

Fig. 9 Velocity profiles of the undisturbed boundary layer in absolute measures (left) and wall units (right).

Brilliant Twins, Nd:YAG, 150 mJ proPuls) generated a light sheet orthogonal to the mean flow and the flat plate. Two cameras (LaVision Flow Master 3S3D with 1280×1024 pixel^2), each on one side of the laser, were directed at an angle of 45° to the area of interest. Each camera was equipped with a teleconverter (Tamron Teleconverter 2x) and a macro telephoto lens (Tamron SP AF DI 180 mm 1:3.5) that gave a final field of view of 32×6 mm with a spatial resolution of the vector field of approximately 0.2 mm. The images were cropped in the vertical image plane during acquisition to exclude uninteresting areas. The spanwise extend of the measurement domain covers the structures of approximately six vanes, due to the large number of vanes in the spanwise direction periodicity can be assumed. A digital frequency generator (Tektronix AFG 3022) serves as interface between the PIV system and the actuators and produces a trigger signal for the PIV system parallel to the input signal of the actuators. The signal was amplified to drive the piezobender using a Trek PZD2000 with maximum voltages of ± 2 kV and maximum current of 400 mA.

An experimental uncertainty of the resulting velocity fields was determined with a correlation accuracy of the software of 0.1 pixels [32] and the assumptions published in [33]. The velocity uncertainty is better than $\Delta(u, v, w) \approx 0.2$ m/s for all velocity components (see also [31]).

The flowfields were measured for the following cases: undisturbed flow, VVGs with static deflection, and dynamic operation for frequencies $f \in [112, 183, 291, 388]$ Hz, $x \in [10, 20, 50] \cdot h$ behind the devices. For each frequency the period was divided into eight even parts ($\varphi \in [0, 45, 90, \ldots, 315]°$) to give phase-locked measurements.

B. Data Processing

The data have been processed using the PIV software LaVision DaVis7. Minor vibrations of the setup were eliminated using a shift correction. This was done by determining small displacements of the reflection line (relative to the first picture of a data set) by a cross-correlation technique and then shifting each image by that amount so that the reflection line is exactly at the same position in each image of the data set. The signal-to-noise ratio of the images is increased substantially by calculating the mean pixel-image of a data set and then subtracting it from every individual image. This eliminates background noise, e.g., due to diffused light reflections.

The images were then correlated using standard PIV approaches (stereo-PIV self-calibration, second-order cross-correlation with decreasing interrogation window size, 50% overlap, window-shifting, window-deformation, and Whittaker reconstruction [31]). Approximately 350 individual flowfields were recorded, averaged, and longitudinal vorticity ω_x was computed from the resulting vector fields. The vortex cores can be found by determining the minimum value of the discriminant of the nonreal eigenvalues of the gradient matrix [34]. To assess the strength of the vortices one pair of counter-rotating vortices was chosen and the longitudinal circulation was computed [Eq. (7)] from the vorticity fields. All data analysis was done with the two vortex structures in the center of the measurement domain:

$$\Gamma_x = \iint \omega_x \, \mathrm{d}y \, \mathrm{d}z \tag{7}$$

IV. Results

A. Turbulent Boundary Layer Without VVGs

Figure 9 shows the distribution of the velocity components u, v and w of the undisturbed boundary layer. The magnitude of the transverse components $v \approx w \approx 0$ indicates that the light sheet was well aligned with the flow. The freestream velocity was $u_\infty =$ 15.4 m/s, this results in a thickness of the boundary layer (at the location 10 heights behind the VVGs) of $\delta = 10.35$ mm (using the 99% criterion), the local Reynolds number is $Re_x = 3.5 \times 10^5$, local Reynolds number based on the momentum thickness $\theta = 1.28$ mm is $Re_\theta \approx 1300$. The boundary conditions were chosen to be similar to the experiments described in [16,21] to achieve comparability. Figure 9 also shows the longitudinal velocity profile in wall units. This indicates that the turbulent boundary layer is well developed and that the measurements are able to analyze the effect of the VVG on the outer boundary layer and the log-law region, whereas the viscous sublayer ($z^+ < 5$) cannot be resolved with this setup. The shear stress velocity u_τ used to calculate wall units is based on an analytical relationship [35]. Table 3 summarizes all boundary-layer parameters of the undisturbed boundary layer. The uncertainties are estimations based on the fact that the exact position of the surface is only known to an accuracy of about ± 0.2 mm due to wall reflections of the laser light sheet.

B. VVGs in Static Operation

Figure 10 shows the streamwise development of the vortex structures for $x \in [10, 20, 50] \cdot h$ in static operation, where pairs of counter-rotating vortices are visible. The vectors highlight the in-plane velocity components v and w, whereas the contour lines indicate the magnitude of the streamwise flow component u. It is clearly visible that in regions where fluid flows down the vortices shift momentum from the outer parts of the boundary layer close to

Table 3 Properties of the turbulent boundary layer (without actuation) at position $x = 10 \cdot h$

Property	Value	Unit
u_∞	15.4	m/s
$\delta_{99\%}$	10.35 ± 0.2	mm
δ^*	1.79 ± 0.2	mm
θ	1.28 ± 0.15	mm
H_K	1.39 ± 0.25	——
Re_x	356'000	——
Re_θ	1305	——
u_τ	0.129	m/s

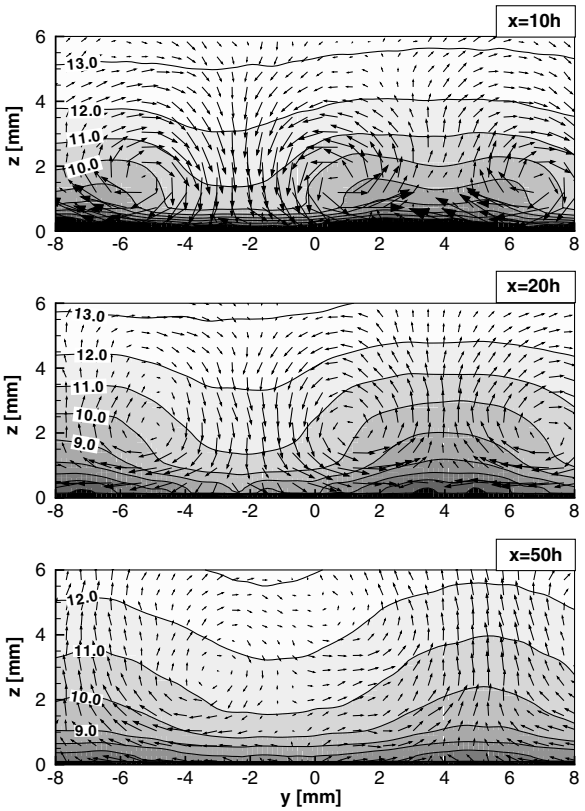

Fig. 10 Streamwise development of the flowfield in static operation for $x = [10, 20, 50] \cdot h$; every third vector is displayed. Contour lines denote streamwise velocity at 1 m/s per contour line; refer to contour labels for absolute values.

the wall and vice versa in regions of upward flow. Thus, the near-wall flow is accelerated in the downward flow regions and decelerated where the fluid flows upwards. In total, the content of the overall momentum in the regions below the vortex cores is typically positively influenced, and therefore such longitudinal vortices are able to prevent separations.

The diametrical dimensions of the vortices increases successively from $x = 10 \cdot h$ up to $x = 50 \cdot h$. They reach their maximum intensity at $x = 20 \cdot h$ and start to decay further downstream. It should be noted that in regions close to the VVGs ($x = 10 \cdot h$), a modulation of the longitudinal velocity is very locally affected and vanishes for larger distances from the wall ($z > 6$ mm), while further downstream (e.g., $x = 50 \cdot h$) the whole thickness of the boundary layer is modulated. The in-plane motion of the vortices almost vanishes in the last section $x = 50 \cdot h$.

C. VVGs in Dynamic Operation

Figure 11 visualizes the transient formation of the vortex structures for $f = 388$ Hz in position $x = 10 \cdot h$. The left-hand side shows the velocity components and the right-hand side depicts the vorticity ω_x. As mentioned, the phase angle $\varphi = 0°$ equals the point in time when the VVGs are fully extracted. The vortices need approximately a quarter-phase to convect into the position $x = 10 \cdot h$. The buildup and decay of the vortices follows a somehow sinusoidal motion and the peak vorticity builds up at $\varphi = 135°$. Note that during the startup motion (phase angles $\varphi = 0$–$135°$) the vortex centers are further apart from the wall, while they start to descend when the vortices decay. This behavior will be discussed in more detail below.

D. Vortex Development

It was shown in [16] that circulation Γ_x is one of the main parameters affecting the ability of a vortex to shift momentum. Therefore, to assess the effectiveness of the devices, the circulation of the vortices was computed as described in the previous section. One pair of counter-rotating vortices was analyzed for each position x, frequency f and phase angle φ, respectively. Figure 12 shows the transient formation $\Gamma/\Gamma_{\text{stat}}$, which is defined as the circulation Γ_x of the dynamically actuated field relative to the circulation of the vortex from the statically deployed vortex generator Γ_{stat} at the same position. The sinusoidal motion of the vortex generators, and hence the development of circulation, is clearly apparent. Note that the peak circulation of the frequencies $f \in [112, 183, 291]$ Hz is about three times higher than the circulation in static operation, but for $f >$ 291 Hz it decreases rapidly. This behavior is consistent to the conclusions in [16,17] that were drawn from measurements of vortex generator jets in a water tunnel: if the transients are slow (low frequencies) the vortices are quasi-static. If the frequencies get higher two things happen: First, due to the inertia of the bulk flow, the VVGs appear suddenly and the bulk flow is not able to create a quasi-steady condition; this transient vortex formation leads to a much higher initial circulation. Second, the old vortices of a preceding period cannot decay fast enough so that the initial circulation increases during the following period. Hence, dynamic operation results in an amplification of the vortex effectiveness for a defined frequency. However, if frequency gets too high and the appearance time of the VVGs is too short, they are thus not able to build up a strong-enough vortex and hence the effectiveness decreases. Therefore, the dynamic operation of the VVGs results in a higher efficiency, if frequency is not too high. Since the analog of the injection time of the dynamic VVGs is closely coupled to the frequency, this behavior is also consistent to the theory of an optimum injection time [5,14] for pulsed vortex generator jets.

Although the vortex might be more intensive during dynamic operation, it was noted before that the position of the vortex core varies during the period. This is an important remark, because the vortices are only effective when they are located close to the wall, due to two effects: First, separation initially starts at the wall; therefore, the momentum close to the wall must be increased, which works better if the vortices are close to the wall. Second, the vortices are more effective close to the wall, because the velocity gradient is higher. Figure 13 shows the transient formation of the position of the vortex centers z relative to the position of the vortices of the static VVGs z_{stat} in position $x = 10 \cdot h$ for the different frequencies. The sinusoidal motion is again clearly apparent. As previously described during vortex buildup, which is a time where the vortices are very intense, the core is located further away from the wall, while during decay they penetrate deeper into the boundary layer. Note that this motion depends considerably less on the frequency than the relative circulation shown in Fig. 12. This behavior is not completely consistent to the findings with fluidic vortex generator jets [16], where the location of the vortex core z during the initial startup is much greater than in quasi-steady state. This might be ascribed to the fact that fluidic vortex generator jets feature a more square-wave function during the period, whereas the dynamic VVGs follow a sinusoidal motion.

In addition to peak circulation, the time-averaged relative circulation shown in Fig. 14 is also important in the determination of whether the dynamic operation is superior to the static one or not (static deflection is denoted as $f = 0$ Hz in the following figures). For the three low-frequency cases the average circulation is greater, indicating that a dynamic operation is more effective than a static deflection of VGs. However, with higher frequencies the dynamic operation of the VVGs becomes ineffective, as described above. It should be noted that only in the most upstream position $x = 10 \cdot h$, are the dynamic VVGs more effective than the statically deflected vane.

This observation is more clearly shown in Fig. 15, as the streamwise development of the time-averaged circulation. In the position $x = 10 \cdot h$, the average circulation of the frequencies $f \in$ [112, 183, 291] Hz is higher than in static operation, as shown above. However, at a position further downstream, the average circulation of the static VVGs increases, whereas the circulation of dynamically operated VVGs continuously decreases. Therefore, dynamic VVGs maybe more suitable for near-field control.

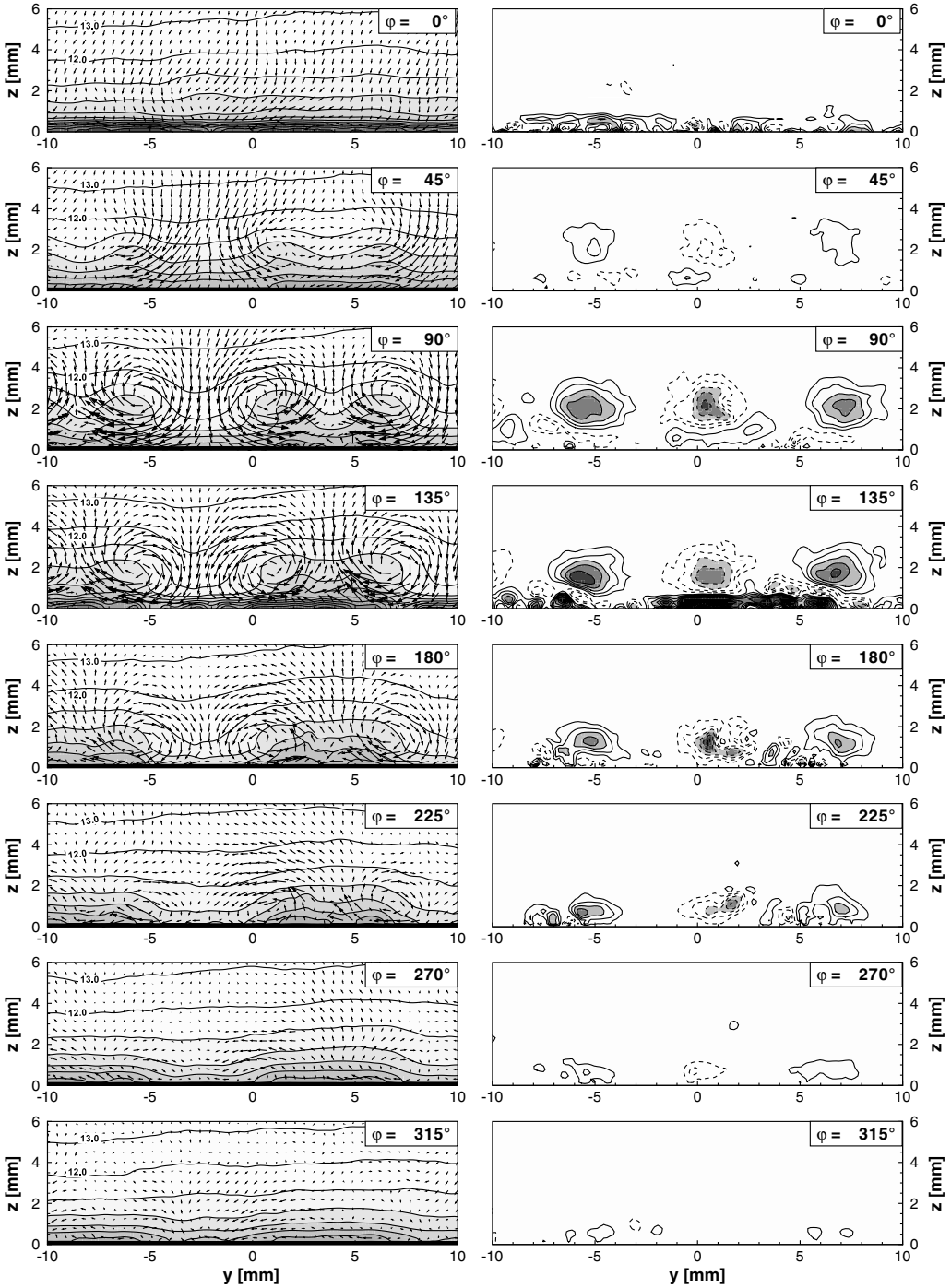

Fig. 11 Evolution of velocity field (left) and vorticity ω_x (right) during dynamic operation with $f = 388$ Hz in position $x = 10 \cdot h$; every third vector is displayed. Contour lines denote streamwise velocity, spacing is 1 m/s per contour line; vorticity contour lines are spaced $\omega_x = \pm 400$ 1/s per line; solid line is positive and dashed line is negative.

E. Turbulence Characteristics

For an analysis of the influence of the VVGs on the turbulence characteristics, probability density distributions (PDFs) of the fluctuations were extracted. In flowfields that follow, a periodic motion the velocities might be dissembled using a triple decomposition $u = \bar{u} + \hat{u} + u'$, where the instantaneous velocity component u is the sum of the mean velocity $\bar{u}$, the periodical fluctuation $\hat{u}$ and the stochastic fluctuation u' [17]. From the flowfields of the PIV measurements, two heights above the surface, $z^+ = 21.8$ and $z^+ = 126.5$, were extracted and then the instantaneous longitudinal component of the velocity u was decomposed into the above mentioned fractions. The spanwise extend for this operation was chosen such that the structures of six vanes are covered, which equals three spanwise wavelengths. Because of the large number of vanes in the spanwise direction (26 at total) periodicity can be assumed. This approach results in the following values:

1) For the undisturbed boundary layer without any actuation: the mean value $\bar{u}_0$ and the stochastic fluctuation u'_0 are observed. Since the basic boundary layer is not periodic, it has no periodic component $\hat{u}_0 = 0$.

2) For the boundary layer influenced by statically deployed VVGs: the mean value $\overline{u_{\text{stat}}}$ and the stochastic fluctuation u'_{stat} are observed. This flowfield is again not periodic, $\hat{u}_{\text{stat}} = 0$.

3) For the boundary layer influenced by dynamic VVGs: the mean value $\overline{u_{\text{VVG}}}$, the periodic fluctuation $\hat{u}_{\text{VVG}}$ and the stochastic fluctuation u'_{VVG} are observed.

Several different kinds of probability densities are shown in Fig. 16; also depicted in the lowermost subfigure is the evolution of

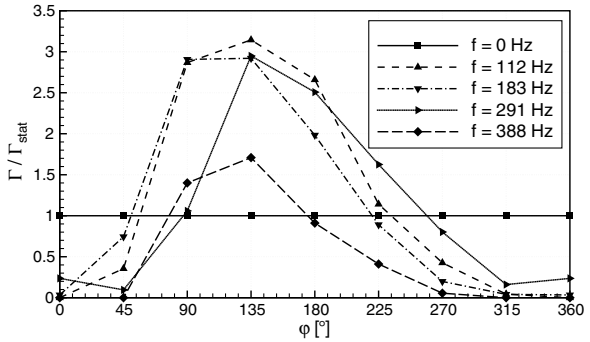

Fig. 12 Relative circulation Γ/Γ_{stat} vs phase angle φ in position $x = 10 \cdot h$ for different frequencies.

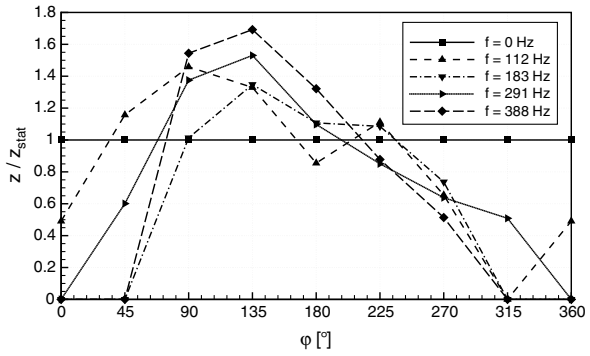

Fig. 13 Relative position z/z_{stat} of vortex centers vs phase angle φ in position $x = 10 \cdot h$.

z_{VVGs} for orientation purposes. It should be noted that the position $x = 20h$ is well apart from the VVGs, so the vortices need some time, which is in this case approximately half a period, to convect downstream until they reach this position.

The upper left part of Fig. 16, entitled dynamic motion, shows the PDF of the instantaneous velocity with VVGs $u_{VVGs}(y, \varphi)$ relative to the mean of the boundary layer without actuation $\bar{u}_0(y)$. The upper right parts titled static deflection and undisturbed boundary layer show the same values for the statically deployed VVGs and the undisturbed boundary layer. They have been calculated with exactly the same approach as the probability densities on the left-hand side, with the difference of course that they do not contain a periodic component. The rightmost subfigure (undisturbed boundary layer) corresponds to the PDF of the stochastic fluctuations (turbulence). The axis of abscissae of all PDFs in the upper row was normalized with the mean of the boundary layer without actuation $\bar{u}_0$.

By definition, because the mean value of turbulence vanishes, the rightmost PDF must be symmetric, whereas the PDFs of statically or dynamically VVGs can be asymmetric, where this asymmetry indicates a change with respect to the undisturbed boundary layer.

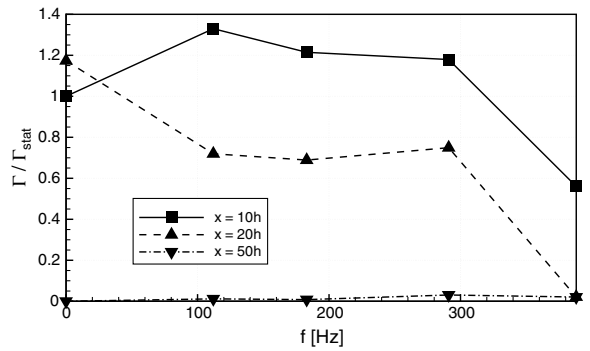

Fig. 14 Time-averaged relative circulation $\bar{\Gamma}/\Gamma_{stat,10 \cdot h}$ vs frequency f for the different streamwise positions $x = [10, 20, 50]h$.

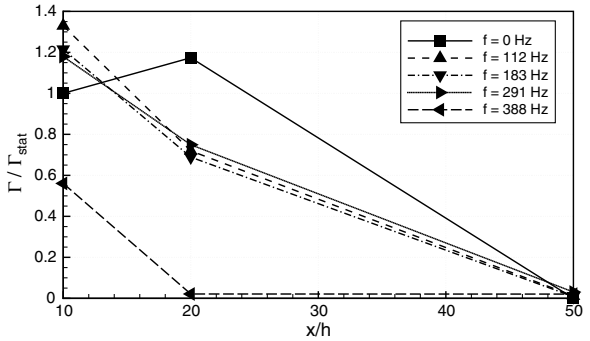

Fig. 15 Time-averaged relative circulation $\bar{\Gamma}/\Gamma_{stat,10 \cdot h}$ vs distance from the point of actuation x/h for the different frequencies.

Note that for the phase angles $\varphi \in 0$–$180°$ the centroid of the PDF distribution is shifted to higher velocities in the case $z^+ = 21.8$ and to smaller velocities for $z^+ = 126.5$. This means that during these phase angles the areas further away from the wall are losing momentum, while the regions close to the wall gain momentum. Hence, the deviation of the centroid is a value for the amount of momentum that was rearranged by the VVGs. Note that this deviation is considerably larger in the case of dynamic motion than for static deflection. This means that, although the time-averaged circulation of dynamic motion in this position $x = 20 \cdot h$ is less than in the case of static deflection (see Fig. 15), the longitudinal velocity close to the wall during dynamic motion is increased by a greater amount.

Furthermore, it can be noted that a sideward shift of the centroid is connected with a decreased peak value of the probability. For example, the cases $\varphi = 0$–$180°$ show a significantly wider distribution. This means that the shift of momentum is closely connected with an increased turbulence (or, better, the turbulence involves larger deviations from the mean value). However, this turbulence is counted relative to the undisturbed boundary layer and hence contains any kind of fluctuation: e.g., large-scale movements of the vortex core.

To separate periodic large-scale movements from stochastic fluctuations, the left part of the lower row of Fig. 16 entitled dynamic motion shows the PDF of the instantaneous velocity with VVGs $u_{VVGs}(y, \varphi)$ relative to the mean value for that specific case and that specific phase angle $\overline{u_{VVGs}(y, \varphi)}$. Again the right parts static deflection and undisturbed boundary layer show the same values for the statically deployed VVGs and the undisturbed boundary layer. This row of PDFs by definition contains only stochastic fluctuations, the centroid of each of the individual PDFs must be located at zero. The rightmost distribution is identically to the corresponding plot in the upper row, because both represent the same case; the fluctuations of the undisturbed boundary layer relative to the mean flow of it are plotted twice here for the sake of a better comparison of the peak height within a single row.

The lower row of PDFs highlights the influence of the VVG motion on the stochastic turbulence. It is clearly visible that none of the PDFs is considerably different from the PDF of the undisturbed boundary layer. Close to the wall at $z^+ = 21.8$, the peak PDF tends to be reduced by the VVGs, which means that larger deviations from the mean velocity are more likely; however, these variations are small and even smaller at the distance ($z^+ = 126.5$) further away from the wall.

In conclusion, it can be stated that the influence of the VVGs is indeed a phenomenon of large-scale momentum transport and it is not an effect on turbulence scales. It must be noted that the PDF distributions for higher frequencies vary slightly more than the highlighted case $f = 112$ Hz. Yet, in any case the variation of the PDF relative to the base boundary layer (representing large-scale periodic motions) is substantially more influenced than the PDF relative to the individual mean value (representing stochastic turbulence). Hence, even for higher frequencies the basic turbulence characteristics of the boundary layer are almost unchanged.

Finally, it can be noted from Fig. 16 that the vortical pulse arrives at the position $x = 20 \cdot h$ (equals 40 mm) at a phasing of approximately

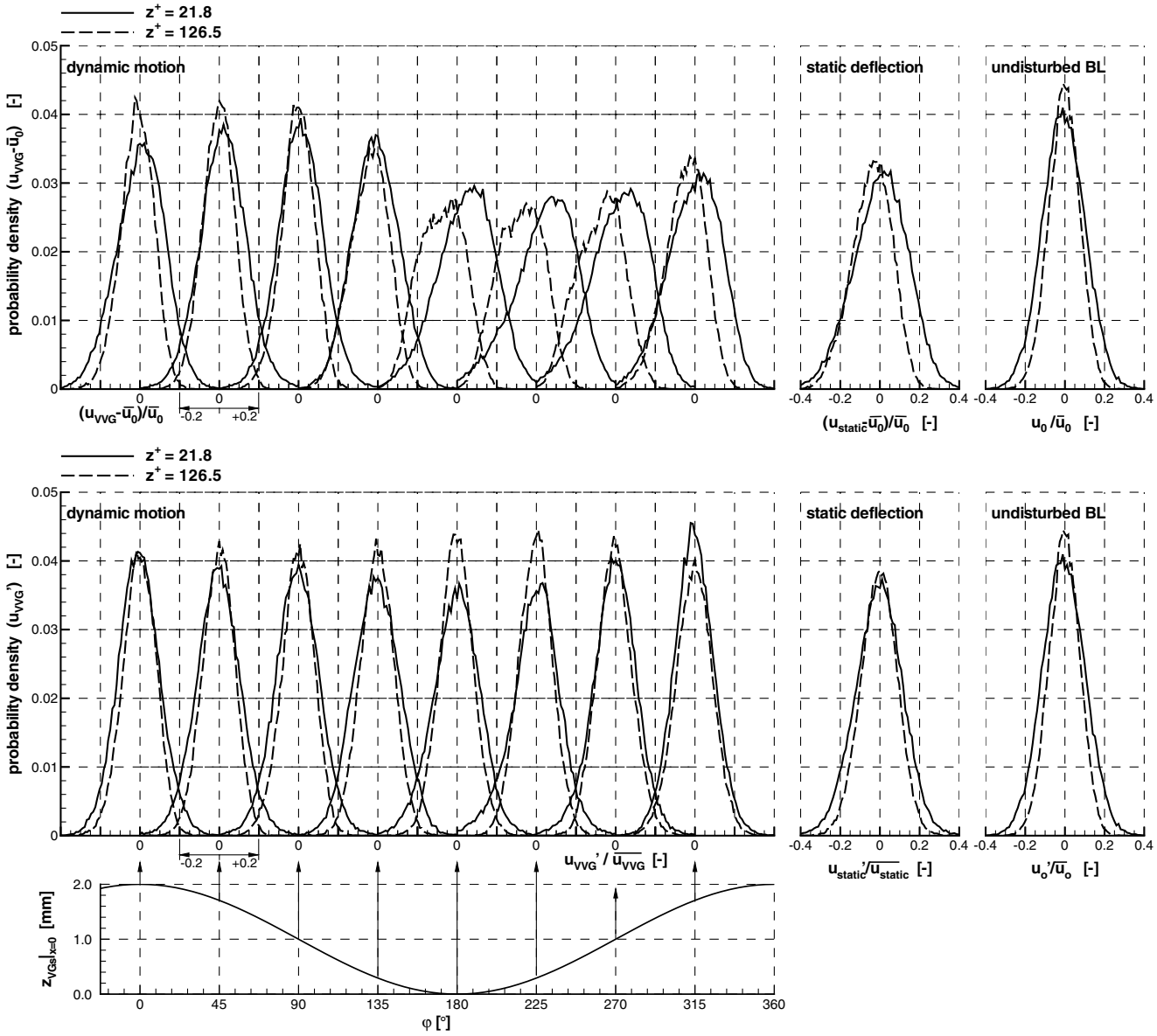

Fig. 16 Temporal evolution of the probability density of the longitudinal velocity relative to the mean flow of the undisturbed boundary layer (upper) and relative to the phase-locked mean value of the individual case (lower) at $x = 20 \cdot h$ for three cases: $f = 112$ Hz, static deflection and the undisturbed boundary layer in two different wall-normal distances z^+. Refer to the text for a more detailed explanation.

$\varphi \approx 140°$. This points a convection velocity of approximately $u =$ 11 m/s out; referring back to Fig. 9, this means that the vortex structure travels approximately with the mean velocity at the tip of the vortex vanes.

V. Conclusions

In this study, a flow control system that consisted of VVGs operated dynamically by means of piezoceramic actuators has been developed. The scope of the study was to analyze the effect of the sinusoidal motion of the VVGs in a frequency range of $f =$ 100–500 Hz on a turbulent boundary layer. The motion was generated by face actuators, which were designed as an actively bending bar. To increase the dynamic displacement of the actuators the eigenfrequency was tuned to the desired operating point by mass clamps. Both VVGs and actuators were integrated into a flat plate, which was placed in a low-speed wind tunnel, where the flowfield was determined by means of a 3C2D stereo-PIV system.

The experimental results demonstrate that dynamic operation is superior to static operation. The peak circulation in a position close behind the VVGs $x = 10 \cdot h$ was over three times higher for frequencies in the range of $f \in$ 100–300 Hz (or $Sr \in 0.07$–0.2) compared with the case of a static deflection. The time-averaged circulation was still up to 20 % higher for dedicated cases. However, the analysis of the downstream development indicated that dynamic vortices decay faster than the statically produced vortices. An analysis of the impact of the VVGs on the turbulence characteristics showed that the effect is mainly due to large-scale momentum rearrangement and that the VVGs do not considerably affect the turbulent scales. Using time-averaged circulation as the assessment factor, a most effective frequency cannot clearly be found: there seems to be a threshold around $Sr \approx 0.25$ above which dynamic actuation becomes more ineffective. In existing literature a Strouhal number of $Sr \approx 0.2$ has been proposed to be a particularly effective one. The analysis presented herein confirms that $Sr \approx 0.2$ is an effective Strouhal number; however, smaller frequencies turn out to have a similar effectiveness.

Acknowledgments

This project was financed internally by the Institut für Strömungsmechanik for the fluid mechanical part and by the Institut

für Faserverbundleichtbau und Adaptronik for the structural mechanics and adaptronics part. The authors like to thank Gregory Cartland Glover from Forschungszentrum Rossendorf in Dresden for proofreading of the interim versions.

References

[1] McCurdy, W. J., "Investigation of Boundary Layer Control of an NACA 16-325 Airfoil by Means of Vortex Generators," United Aircraft Corp., Research Department, Rept. M-15038-3, 1948.

[2] Shabaka, M. A. I. M., Mehta, R. D., and Bradshaw, P., "Longitudinal Vortices Imbedded in Turbulent Boundary Layers, Part 1. Single Vortex," *Journal of Fluid Mechanics*, Vol. 155, 1985, pp. 37–57. doi:10.1017/S0022112085001707

[3] Pauley, W. R., and Eaton, J. K., "Experimental Study of the Development of Longitudinal Vortex Pairs Embedded in a Turbulent Boundary Layer," *AIAA Journal*, Vol. 26, No. 7, 1988, pp. 816–823. doi:10.2514/3.9974

[4] Godard, G., and Stanislas, M., "Control of a Decelerating Boundary Layer. Part 1: Optimization of Passive Vortex Generators," *Aerospace Science and Technology*, Vol. 10, No. 3, 2006, pp. 181–191. doi:10.1016/j.ast.2005.11.007

[5] Logdberg, O., "Turbulent Boundary Layer Separation and Control," Ph.D. Thesis, Royal Institute of Technology, KTH, Stockhom, 2008.

[6] Barrett, R., and Farokhi, S., "Subsonic Aerodynamics and Performance of a Smart Vortex Generator System," *Journal of Aircraft*, Vol. 33, No. 2, 1996, pp. 393–398. doi:10.2514/3.46950

[7] Lin, J. C., Robinson, S. K., and McGhee, R. J., "Separation Control on High-Lift Airfoils via Micro-Vortex Generators," *Journal of Aircraft*, Vol. 31, No. 6, 1994, pp. 1317–1323. doi:10.2514/3.46653

[8] Wallis, R. A., "The Use of Air Jets for Boundary Layer Control," Aeronautical Research Labs., Aero-Note-110, 1952.

[9] Wallis, R. A., "A Preliminary Note on a Modified Type of Air Jet for Boundary Layer Control," Aeronautical Research Council, TR 513, 1960.

[10] Johnston, J. P., and Nishi, M., "Vortex Generator Jets—Means for Flow Separation Control," *AIAA Journal*, Vol. 28, No. 6, 1990, pp. 989–994. doi:10.2514/3.25155

[11] Compton, D. A., and Johnston, J. P., "Streamwise Vortex Production by Pitched and Skewed Jets in a Turbulent Boundary Layer," *AIAA Journal*, Vol. 30, No. 3, 1992, pp. 640–647. doi:10.2514/3.10967

[12] McManus, K., Legner, H. H., and Davis, S. J., "Pulsed Vortex Generator Jets for Active Control of Flow Separation," 25th AIAA Fluid Dynamics Conference, AIAA Paper 95-2218, New Orleans, 1994.

[13] Tilmann, C. P., Langan, K. J., Betterton, J. G., and Wilson, M. J., "Characterization of Pulsed Vortex Generator Jets for Active Flow Control," U.S. Air Force Research Lab., AFRL-VA-WP-TP-2003-336, Wright-Patterson AFB, OH, 2003.

[14] Johari, H., and Rixon, G. S., "Effects of Pulsing on a Vortex Generator Jet," *AIAA Journal*, Vol. 41, No. 12, 2003, pp. 2309–2315. doi:10.2514/2.6836

[15] Scholz, P., Ortmanns, J., Kähler, C. J., and Radespiel, R., "Influencing the Mixing Process in a Turbulent Boundary Layer By Pulsed Jet Actuators," *New Results in Numerical and Experimental Fluid Mechanics*, edited by V. H.-J. Rath, C. Holze, H.-J. Heinemann, and R. Henke, Springer, New York, 2006, pp. 265–272.

[16] Ortmanns, J., Bitter, M., and Kähler, C. J., "Dynamic Vortex Structures for Flow-Control Applications," *Experiments in Fluids*, Vol. 44, No. 3, 2008, pp. 1–12.

[17] Ortmanns, J., and Kähler, C., "The Effect of a Single Vortex Generator Jet on the Characteristics of a Turbulent Boundary Layer," *International Journal of Heat and Fluid Flow*, Vol. 28, No. 6, 2007, pp. 1302–1311. doi:10.1016/j.ijheatfluidflow.2007.06.006

[18] Cattafesta, L. N., III, Garg, S., and Shukla, D., "Development of Piezoelectric Actuators for Active Flow Control," *AIAA Journal*, Vol. 39, No. 8, 2001, pp. 1562–1568. doi:10.2514/2.1481

[19] Osborn, R., Kota, S., Hetrick, J., Geister, D., Tilmann, C., and Joo, J., "Active Flow Control Using High-Frequency Compliant Structures," *Journal of Aircraft*, Vol. 41, No. 3, 2004, pp. 603–609. doi:10.2514/1.111

[20] Seshagiri, A., Cooper, E., and Traub, L. W., "Effect of Vortex Generators on an Airfoil at Low Reynolds Numbers," *Journal of Aircraft*, Vol. 46, No. 1, 2009, pp. 116–122. doi:10.2514/1.36241

[21] Scholz, P., Ortmanns, J., Kähler, C. J., and Radespiel, R., "Performance Optimization of Pulsed Jet Actuator Arrays," *CEAS/KATnet Conference on Key Aerodynamic Technologies*, Bremen, Germany, 20–22 June 2005.

[22] Wei, S., and Ning, T., "Bursting Frequency in Turbulent Boundary Layers," *Acta Mechanica Sinica*, Vol. 4, No. 4, 1988, pp. 291–296. doi:10.1007/BF02486661

[23] Kim, H. T., Kline, S. J., and Reynolds, W. C., "The Production of Turbulence Near a Smooth Wall in a Turbulent Boundary Layer," *Journal of Fluid Mechanics*, Vol. 50, No. 1, 1971, pp. 133–160.

[24] Blackwelder, R. F., and Haritonidis, J. H. "Scaling of the Bursting Frequency in Turbulent Boundary Layers," *Journal of Fluid Mechanics*, Vol. 132, No. 1, 1983, pp. 87–103.

[25] Wu, J., Lu, X., Denny, A., Fan, M., and Wu, J., "Post-Stall Flow Control on an Airfoil by Local Unsteady Forcing," *Journal of Fluid Mechanics*, Vol. 371, 1998, pp. 21–58. doi:10.1017/S0022112098002055

[26] Ho, C., and Huerre, P., "Perturbed Free Shear Layers," *Annual Review of Fluid Mechanics*, Vol. 16, No. 1, 1984, pp. 365–422. doi:10.1146/annurev.fl.16.010184.002053

[27] Wilkie, K., Byant, R. G., High, J. W., Fox, R. L., Hellbaum, R. F., Jalink, A., Little, B. D., and Mirick, P. H., "Low-Cost Piezocomposite Actuator for Structural Control Applications," *7th International Symposium on Smart Structures and Materials*, SPIE, Bellingham, WA, 2000.

[28] Monturet, V., and Nogarede, B., "Optimal Dimensioning of a Piezoelectric Bimorph Actuator," *European Physical Journal: Applied Physics*, Vol. 17, 2002, pp. 107–118. doi:10.1051/epjap:2002003

[29] Crawley, E. F., and Anderson, E. H., "Detailed Models of Piezoceramic Actuation of Beams," *Journal of Intelligent Material Systems and Structures*, Vol. 1, 1990, pp. 4–25. doi:10.1177/1045389X9000100102

[30] Beitz, W., Grote, K., and Dubbel, H., *Taschenbuch fur den Maschinenbau*, Springer–Verlag, Berlin, 1983.

[31] Raffel, M., Willert, C., Wereley, S. T., and Kompenhans, J., *Particle Image Velocimetry: A Practical Guide*. Springer–Verlag, Berlin, 2007.

[32] Stanislas, M., Okamoto, K., Kahler, C., and Westerweel, J., "Main Results of the Second International PIV Challenge," *Experiments in Fluids*, Vol. 39, No. 2, 2005, pp. 170–191. doi:10.1007/s00348-005-0951-2

[33] Prasad, M. K., "Stereoscopic Particle Image Velocimetry," *Experiments in Fluids*, Vol. 29, 2000, pp. 103–116. doi:10.1007/s003480000143

[34] Vollmers, H., "Detection of Vortices and Quantitative Evaluation of Their Main Parameters from Experimental Velocity Data," *Measurement Science and Technology*, Vol. 12, 2001, pp. 1199–1207. doi:10.1088/0957-0233/12/8/329

[35] Truckenbrodt, E., *Stroemungsmechanik*, Springer–Verlag, Berlin, 1968.

E. Gutmark
Associate Editor